LDV VELOCITY MEASUREMENTS IN THIN LAMINAR BOUNDARY LAYERS, SEPARATED AND UNSEPARATED, AND COMPARISON WITH NUMERICAL COMPUTATIONS

G. DEGREZ
ASSISTANT, U. LIBRE DE BRUXELLES, BELGIUM

AND

C.H. BOCCADORO & J.F. WENDT
VON KARMAN INSTITUTE FOR FLUID DYNAMICS
B-1640 RHODE SAINT GENÈSE, BELGIUM

Abstract

Single-component LDV velocity measurements were obtained in separated and unseparated 2D thin laminar boundary layers for low- and high speed flow conditions. The low speed case was that of flow over an elliptic cylinder of axis ratio 4:1; the high speed case was that of an incident shock wave laminar boundary layer interaction. For the latter flow, the Mach number was 2.20 and the Reynolds number 1.10^6. In both cases, the flow was laminar and was proved nominally 2D. Velocity measurements were obtained within 0.1 mm from the wall both at high and low speed in unseparated and separated regions, and showed evidence of reverse flow.

An implicit scheme to solve the compressible Navier-Stokes equations was coded to predict the shock wave/boundary layer interaction. Comparison with the experimental data shows excellent agreement in terms of pressure distributions, position of separation and reattachment and velocity profiles.

Nomenclature

c	velocity of sound
c_f	skin friction coefficient
e	internal energy
E	total internal energy
L'	ellipse half-perimeter
M	Mach number
p	pressure
Re	Reynolds number
s	distance along ellipse surface
t	time
T	temperature
u,v,w	velocity components
$\vec{V}$	velocity vector
x,y,z	cartesian coordinates
x_{sh}	shock impingement distance
γ	specific heat ratio
ξ,η,ζ	non dimensional curvilinear coordinates
μ	viscosity
ρ	density
τ	time

Subscripts

f	final	reatt	reattachment
min	minimum	sep	separation
		∞	free stream

Introduction

The rapid development of computational methods for solving the Navier-Stokes equations has stimulated a renewed interest in laminar separated flows at high Reynolds numbers. Indeed, for the purpose of evaluating the qualities of the various computational schemes, laminar test cases are preferable to turbulent cases because of the uncertainty associated with turbulence modeling. Unfortunately, laminar separated flows are often unstable and only very few data sets are available [1,2]. Three dimensional flow data are particularly lacking.

The von Karman Institute has undertaken a program of studies to provide a complete data set on a 3D skewed shock wave laminar boundary layer interaction (Fig. 1). A necessary ingredient of the data set is the velocity distribution in the interaction, together with existing surface flow data [3,4]. Obtaining these velocity measurements represents a major experimental challenge because of the combination of high speed, three dimensionality, the need for high spatial resolution, and the proximity of solid surfaces.

The experimental technique selected to perform these measurements is Laser Doppler Velocimetry (LDV) whereby fluid velocities are measured by observing the doppler shift in the frequency of laser light scattered by small particles moving with the fluid. The main advantage of LDV over other common techniques for measuring velocities (pressure probes or hot wire anemometry) is that no probe needs be inserted in the flow. This factor is particularly attractive for measurements in separated and/or compressible flows. Furthermore, LDV does not require calibration. The relation between the doppler frequency and particle velocity is exact and linear, in contrast with the non linearity of the hot wire anemometer. On the other hand, the measured velocity is that of the scattering particles, not the fluid itself. For the measurements to be representative of the fluid velocity field, it must be ensured that the slip velocity of the particles is zero or at least small with respect to the measured velocity even in strong acceleration regions.

A step-by-step approach to the high speed 3D problem was chosen. In the first step, velocity measurements were performed in the low speed flow over an elliptic cylinder. The flow conditions provided thin laminar boundary layers separating to form a laminar bubble downstream of the cylinder. The problems addressed by this step were the need of high spatial resolution and the proximity of solid surfaces. A second step is given by the study of the 2D incident shock wave laminar boundary layer interaction, which adds the complication of high speed to the previous step. Despite it now being a classical flow, very few velocity data exist because of the limitations of the classical measurement techniques. The third step will add the third dimension to the problem. The results of the two first steps will be presented in this paper.

Simultaneously with the experimental program, a computer code was developed to solve the compressible Navier-Stokes equations based on an implicit ap-

proximate factorization scheme [5]. Its purpose is to provide numerical results for comparison with the experimental data, particularly for the 3D geometry (Fig.1). Preliminary results obtained on a coarse mesh [6] are encouraging. They qualitatively reproduce all features of the flow field. In this paper, comparisons of experimental data with numerical results obtained using this code are presented for the 2D incident shock wave laminar boundary layer interaction. In addition, the low speed velocity data are compared with results of a boundary layer computation using the scheme presented in [7] for the attached region of the flow.

To summarize, the aim of the study presented here was twofold. First, the possibility of performing velocity measurements in 2D separated laminar boundary layers was to be demonstrated, both in a low and in a high speed flow. Secondly, the ability of a Navier-Stokes code to predict an interactive separated flow was to be assessed.

Experimental program

The detailed experimental program upon which this paper is based, is fully described in [8] for the low speed experiment and in [9] for the high speed experiment. The present description is thus appropriately abbreviated.

Low speed experiments

Wind tunnel and test condifuration. The experiments were carried out in a small blowdown wind tunnel having a contraction ratio of 4:1 to ensure uniformity of the flow. Account was taken of the boundary layer growth along the tunnel walls to design the test section so that its effective size was 12 cm×12 cm. By adjusting the supply pressure, the flow velocity could be varied from a few centimeters per second to 5 ms^{-1}. Uniformity of the flow was checked over that range. The facility, together with the experimental setup, is shown in Fig.2.

The model consisted of an elliptic cylinder having a major axis of 4 cm and a minor axis of 1 cm (4:1) which spanned the test section. These dimensions not only provided thin laminar boundary layers but also kept the blockage ratio within an acceptable value (2.5%). Two dimensionality of the flow over this model was carefully checked. Two flow conditions were studied : $u_\infty=1$ ms^{-1} and 2 ms^{-1} yielding Reynolds numbers based on the minor axis of 625 and 1350 respectively. This ensured that the flow remained laminar over the entire length of the ellipse and in the separation bubble. For the highest Reynolds number, an estimate of the boundary layer thickness at the trailing edge of the ellipse is 2.7 mm, which is comparable to the boundary layer thickness in the high speed experiment.

Measurement technique. The velocity measurements were performed with a single velocity component dual beam (fringe mode) laser doppler velocimeter using a 15 mW helium/neon laser. The setup is shown in Fig.2 and its parameters are listed in table 1. The complete instrument (optics and electronics) is described in [8]. The LDV system was installed on a microcomputer controlled traversing mechanism having a precision of 0.02 mm in each direction. Seeding was produced by a Norgen microfog lubricator which utilized mineral oil to generate sub-micron particles of liquid [10].

High speed experiment

Wind tunnel and test configuration. The experiments were carried out in the S-1 wind tunnel of the von Karman Institute. It is a continuous, closed circuit, Ackeret type tunnel with a 40 cm×40 cm cross

section. The range of stagnation pressure is from 0.1 to 0.3 bar. The Mach number 2.25 nozzle was selected to perform the experiments. This gives unit Reynolds numbers in the range 10^6 to $3\cdot10^6$ m^{-1}. It is equipped with shadow and schlieren systems which were used for qualitative analysis of the flow field.

A schematic of the experimental configuration is shown in Fig.3. The incident shock wave was generated by a sting mounted wedge, which had a span of 36 cm and a length of 27.5 cm. The flat plate has a span of 32 cm, a length of 23.5 cm and a sharp leading edge with a thickness of less than 0.1 mm. The wedge, located 90 mm above the plate, was positioned so that the distance between the incident shock location on the plate boundary layer to the plate leading edge (x_{sh}) was 80 mm.

Side plates could be fixed at several spanwise distances from the plate centerline in order to make a systematic study of the two dimensionality of the flow field. The experiments were carried out with a stagnation pressure of 0.1 bar giving a Reynolds number based on x_{sh} of 10^5. The total temperature was always around 20°C, thus the models were at near adiabatic wall temperatures for all tests.

Surface pressure measurements. The flat plate was instrumented with a row of 31 pressure taps at the centerline. In addition, there were some pressure taps off center to check the uniformity of the pressure distrutions. The pressure tappings were sampled using 12 port scanivalves equipped with a .5 psi Statham transducer.

Velocity measurements. The setup for the high speed velocity measurements was very similar to that for the low speed experiment. Laser system parameters were changed. A 4 watt argon-ion laser was used as light source and forward scattering was used exclusively. The parameters of the LDV setup are shown in table 1 together with the parameters for the low speed experiment. As can be observed the probe volume is larger for the high speed experiment to maintain an acceptable number of fringes and output frequency (not above say 90 MHz). It is, however, still small enough to ensure appropriate spatial resolution. Details concerning the setup and instrumentation can be found in [9]. To minimize reflection problems from the surface, the plane containing the incoming laser beams was set at an incidence of 4.5°, receiving optic was placed 10° off-axis and the surfaces of the plate and wedge were painted flat black.

Laminarity of the flow. For a proper comparison with numerical results, the laminarity of the flow should be ensured. Ginoux [12] proposed a criterion based on the difference of variation of upstream influence with Reynolds number for laminar and transitional flows. Upstream influence increases with increasing Reynolds number for laminar flows; whereas the opposite is true for turbulent flows. Burgio [11] showed that for conditions identical to those chosen for the present experiments, the flow was fully laminar.

Computational method

The theoretical prediction of the high speed flow was obtained by numerically solving the time-dependent Navier-Stokes equations for the 2D flow of a compressible fluid. The hypotheses used in connection with the equations include the perfect gas assumption, constant specific heats and Prandtl number, the Sutherland viscosity law and Stokes' assumption (no bulk viscosity). To account for arbitrary geometries and enhance numerical accuracy and efficiency, coordinate mappings are used which bring all body surfaces into coordinate surfaces and cluster grid

points near the walls. The Navier-Stokes equations then have to be transformed to an arbitrary curvilinear space ξ, η, τ defined by the coordinate mapping. Performing this transformation while retaining the conservation form [13] yields the following equations, which are not much more complicated than the original cartesian set. It should be noted that the equations are in non dimensional form, the normalizing quantities being ρ_∞ for density, c_∞ for velocity, c_∞^2 for total energy, p_∞ for pressure, T_∞ for temperature, a characteristic length L for distances and L/c_∞ for time. For the present computation, the c characteristic length was the shock impingement distance x_{sh} :

$$\frac{\partial \hat{q}}{\partial \tau} + \frac{\partial \hat{f}}{\partial \xi} + \frac{\partial \hat{g}}{\partial \eta} = \frac{1}{Re}\left[\frac{\partial \hat{\sigma}}{\partial \xi} + \frac{\partial \hat{\theta}}{\partial \eta}\right] \qquad (1)$$

where

$$\hat{q} = J\begin{pmatrix}\rho \\ \rho u \\ \rho v \\ \rho E\end{pmatrix} \qquad \hat{f} = \xi_t\hat{q} + J(\xi_x\vec{F}+\xi_y\vec{G})$$
$$\hat{g} = \eta_t\hat{q} + J(\eta_x\vec{F}+\eta_y\vec{G}) \qquad (2)$$

and J is the Jacobian of the inverse transformation, $J = \frac{\partial(x,y)}{\partial(\xi,\eta)}$:

$$\vec{F} = \begin{pmatrix}\rho u \\ \frac{p}{\gamma} + \rho u^2 \\ \rho uv \\ u\left(\rho E + \frac{p}{\gamma}\right)\end{pmatrix} \qquad \vec{G} = \begin{pmatrix}\rho v \\ \rho uv \\ \frac{p}{\gamma} + \rho v^2 \\ v\left(\rho E + \frac{p}{\gamma}\right)\end{pmatrix} \qquad (3)$$

The viscous flow vectors $\hat{\sigma}$ and $\hat{\theta}$ are given in Appendix A. These vectors can be split into various vectors involving derivatives with respect to one coordinate only, i.e., $\hat{\sigma} = \overset{(\xi)}{\sigma} + \overset{(\eta)}{\sigma}$; $\hat{\theta} = \overset{(\xi)}{\theta} + \overset{(\eta)}{\theta}$

$$Re = \frac{\rho_\infty L c_\infty}{\mu_\infty} = \frac{Re_\infty}{M_\infty} , \qquad E = e + \frac{u^2 + v^2}{2}$$

and the equation of state reads

$$\rho e = \frac{p}{\gamma(\gamma-1)} = \frac{\rho T}{\gamma(\gamma-1)}$$

A single step temporal scheme for advancing the solution of Eq.(1) is [14] :

$$\Delta\hat{q}^n = \theta\Delta\tau \frac{\partial}{\partial\tau}\Delta\hat{q}^n + \Delta\tau \frac{\partial\hat{q}^n}{\partial\tau} \qquad (4)$$

The trapezoidal rule scheme is characterized by $\theta = 1/2$, whereas $\theta = 1$ yields the Euler implicit scheme.
Inserting (1) in (4), we obtain, with $\theta = 0$ for the terms $\overset{(\eta)}{\sigma}$ and $\overset{(\xi)}{\omega}$:

$$\Delta\hat{q}^n = \theta\Delta\tau\left[\frac{\partial}{\partial\xi}\left(-\Delta\hat{f}+\frac{1}{Re}\Delta\overset{(\xi)}{\sigma}\right) + \frac{\partial}{\partial\eta}\left(-\Delta\hat{g}+\frac{1}{Re}\Delta\overset{(\eta)}{\theta}\right)\right]$$
$$+ \left[\Delta\tau \frac{\partial}{\partial\xi}\left(-\hat{f}+\frac{\hat{\sigma}}{Re}\right) + \frac{\partial}{\partial\eta}\left(-\hat{g}+\frac{\hat{\theta}}{Re}\right)\right] \qquad (5)$$

It is possible to linearize locally this expression by developing Δf, Δg as a function of Δq :

$$\Delta\hat{f} = \frac{\partial\hat{f}}{\partial\hat{q}}\Delta\hat{q} + O(\Delta\tau^2) = \hat{F}\Delta\hat{q} + O(\Delta\tau^2)$$
$$\Delta\hat{g} = \frac{\partial\hat{g}}{\partial\hat{q}}\Delta\hat{q} + O(\Delta\tau^2) = \hat{G}\Delta\hat{q} + O(\Delta\tau^2) \qquad (6)$$

$\hat{F}$ and $\hat{G}$ are given in Appendix B.

Similarly, the viscous terms can be linearized as :

$$\Delta\hat{\sigma}^{(\xi)} = \hat{S}\Delta\hat{q} + O(\Delta\tau^2) \quad ; \quad \Delta\hat{\theta}^{(\eta)} = \hat{T}\Delta\hat{q} + O(\Delta\tau^2) \qquad (7)$$

With these linearizations, Eq.(5) becomes :

$$\left[I+\theta\Delta\tau\left[\frac{\partial}{\partial\xi}(\hat{F}-\frac{\hat{S}}{Re}) + \frac{\partial}{\partial\eta}(\hat{G}-\frac{\hat{T}}{Re})\right]\right]\Delta\hat{q}$$
$$= \Delta\tau\left[\frac{\partial}{\partial\xi}(-\hat{f}+\frac{\hat{\sigma}}{Re}) + \frac{\partial}{\partial\eta}(-\hat{g}+\frac{\hat{\theta}}{Re})\right] \qquad (8)$$

and this equation is then factorized to yield the final form of the computational algorithm :

$$\left[I+\theta\Delta\tau\frac{\partial}{\partial\xi}(\hat{F}-\frac{\hat{S}}{Re})\right]\left[I+\theta\Delta\tau\frac{\partial}{\partial\eta}(\hat{G}-\frac{\hat{T}}{Re})\right]\Delta\hat{q}$$
$$= \Delta\tau\left[\frac{\partial}{\partial\xi}(-\hat{f}+\frac{\hat{\sigma}}{Re}) + \frac{\partial}{\partial\eta}(-\hat{g}+\frac{\hat{\theta}}{Re})\right] \qquad (9)$$

Fourth order conservative damping terms [15] are appended to the right-hand side of (9) to damp short wavelengths that are not dissipated by the implicit scheme [14].

The computation was performed on a rectangular mesh of 50×36 points. It was uniform in the streamwise direction with $\Delta x = 0.05$ and stretched exponentially normal to the wall over the first 30 points, then uniform. The first point in the normal diameter was located at $y = 9 \cdot 10^{-4}$ which corresponds to a physical value of 0.072 mm ($\sim\delta/20$). The computational domain is shown in Fig.4.

The upstream boundary conditions (boundary I) were prescribed as their uniform free stream values since the upstream flow was supersonic. The outer boundary conditions (boundary II) were also prescribed as being their values in the inviscid field given by oblique shock wave theory. The outgoing boundary (boundary III) was positioned far enough downstream ($x/x_{sh} = 2.3$) to set all streamwise gradients to zero. Boundary IV was treated in two ways : upstream of the plate, symmetry conditions were applied whereas on the plate, the usual no slip conditions were imposed together with the conditions of no normal temperature gradient (adiabatic wall) and no normal pressure gradient. The latter condition is a simplified expression of the local normal momentum equation valid for high Reynolds number flows as indicated by Peyret & Viviand [13].

On a Digital Equipment Corporation VAX 11 computer 30 s per time step were required and less than 200 iterations were needed to obtain convergence starting from an initially uniform flow field.

Results and discussion

Low speed experiment-ellipse

The experiments were conducted in two series. In the first series, no Bragg cells were used, which did not allow the resolution of the flow direction. In this series of measurements, only the problem of the resolution of the measurements was addressed under various model conditions and LDV operating modes. In all cases, only time averaged velocity measurements were performed.

First, the velocities were measured using the forward scatter mode with various model/tunnel conditions. In particular, the effects of painting the surfaces with a matt black paint to avoid reflections and covering the tunnel walls to avoid external light were studied. Figure 5 shows results obtained under these various conditions. As can be observed, the same velocity values were recorded in all measurement cases. It was observed that painting the model resulted in a marked reduction of reflections from the

surface and as associated improvement in the signal-to-noise ratio near the surface.

Figure 5 shows a velocity distribution at a station close to the ellipse leading edge (x=3.24mm) where the boundary layer thickness is small (less than 1 mm). It exemplifies one of the problems in the measurements : determining the zero vertical location. Indeed, there obviously exists a zero shift in the vertical scale of the figure since at the wall, the velocity must be zero to satisfy the no slip condition. Fortunately, laminar velocity profiles display a large nearly linear region and it is therefore easy to find the wall position by extrapolation of the velocity profiles. Once this has been done at one point, the coordinates of any point in the field can be known within the accuracy of the traversing mechanism (admittedly, slight hysteresis can occur). In Fig.6, the results of the measurements performed in the backscatter mode are compared with measurements performed in the forward scatter mode. As can be seen, they are nearly identical proving that the backscatter technique may also be used to perform measurements close to a solid surface. The first measurement point lies at 0.08 mm from the wall for both forward and backscatter modes.

In a second series of measurements, Bragg cells were used to resolve the flow direction and evaluate the measurement problems in the separated region. The Bragg cell frequency was 1.3 MHz. Figure 7 shows a velocity profile measured in these conditions at a location close to the ellipse trailing edge where the reverse flow region is extended. Again, measurements could be performed within 0.05 mm from the wall. The reverse flow region thickness is here 0.65 mm. Measurements were also performed in the wake 10 and 15mm downstream of the trailing edge. The velocity profile shape 15 mm from the trailing edge (Fig.8) suggests that the flow is still laminar, the reverse flow region being 2 mm thick.

To compare the low speed velocity measurements with a boundary layer computation, attention was restricted to the attached flow stations. Since the second series of measurements had shown that the flow was already separated at the ellipse mid chord, only stations 1-5 are shown in Fig.9. The boundary layer computations used the code developed by Arina et al. [7]. The outer velocity distribution was given by potential flow theory. As can be seen, the agreement is good except near the leading edge. In this region, as discussed by Peyret & Viviand [13], the viscous inviscid coupling is strong at this intermediate Reynolds number (1300). It may appear surprising that separation takes place upstream of the mid chord whereas the boundary layer computation yields $s_{sep}/L'=$ 0.823 (value confirmed in [16] $s_{sep}/L'=0.84$). This discrepancy is due to the viscous/inviscid interaction. A similar behaviour was observed by Schubauer [17,18] with an elliptic cylinder of ratio 2.95:1.

High speed experiment - Shock wave boundary layer interaction

Schlieren visualization. A visualization of the flow field studied is shown in Fig.10. The whole structure of the flow can be observed : first the compression wave caused by the viscous/inviscid leading edge interaction, then the compression waves caused by the thickening of the boundary layer which eventually separates. At the impingement point, the shock is reflected as an expansion wave by the shear layer to ensure pressure continuity. Downstream, reattachment of the boundary layer together with the associated compression waves can be observed.

Pressure distribution - Two dimensionality
The two dimensionality of the flow was evaluated in the first part of the high speed experiment. In many experimental studies, it is assumed that transversal uniformity of the flow properties over a certain region ensures two dimensionality. Although this is a necessary condition, it appears not to be sufficient [19]. The accepted sufficient condition is that changes in spanwise extremities of the model (e.g. introducing side-plates) do not affect the flow properties in the centerline; therefore, pressure distributions were measured with thin, triangular side plates being systematically introduced at various distances from the centerline (Fig.11). The work was modelled after Lewis' work with a compression corner [20]. In each instance the aspect ratio (AR) is defined by the ratio of the span between side plates with the shock impingement distance x_{sh}. It was observed that pressure distributions are nearly identical for AR's of 2.5 and greater, thereby satisfying the above two dimensionality criterion. Removing the side plates at AR=4 produces a slightly different pressure distribution, however, since the basic character of the distribution had not changed, the flow could still be considered nominally 2D. Side plate removal was necessary to facilitate the LDV measurements. Let us finally notice that for the compression corner geometry [20] the 2D limit is achieved for much small AR's (∿1) which supports the belief that the situations with incident oblique shock are more susceptible to finite span effects.

Velocity measurements. Velocity measurementd were performed slightly (20 mm) off-centerline because the seeding generator produced a higher particle density along that line. Since the flow was laminar, only average velocity measurements were performed. The Bragg cell frequency was set to 6 MHz allowing an entire profile to be measured at one time. Figure 12 shows the experimental velocity profiles at three stations across the interaction from upstream of its start to downstream of reattachment.

The figure shows that velocity measurements could be performed within 0.1 mm from the plate both in the attached and separated flow regions. Both up- and downstream of the interaction, velocity profiles exhibit the characteristic Blasius shape. The positions of the points of separation and reattachment can be estimated from the schlieren visualization. The values $(x_{sep}/x_{sh}=0.775, x_{reatt}/x_{sh}=1.250)$ are reported in Fig.11 and they match profile data [9].

In the separated region, negative velocities are measured indicating the presence of reverse flow. These negative velocities are always small with the maximum measured value (-22 ms^{-1}) recorded at $x/x_{sh}=$ 1.000. This maximum negative velocity value represents only 4.1% of the free stream velocity.

It can be noticed that a kink appears in the velocity distribution of the separated profiles at u/u_∞ =.05. This kink was also observed in the recent work of Baroth and Holt [2] and it may be the results of local flow unsteadiness.

Computations and comparison with experimental results

The computer code was first validated by computing the incident shock wave boundary layer interaction studies of [1] for which a number of reference computations exist. Figure 13 shows the skin friction distribution over the plate compared with the experimental values and McCormack's computation [21]. The skin friction coefficient was chosen as the test variable because it is most sensitive.

The code was then used with the studied experimental conditions, i.e., $M_\infty=2.15$, $Re_\infty=10^5$, $T_\infty=149°K$ and an overall pressure rise of $p_f/p_\infty=1.55$. It can be noticed that the Mach number value is slightly lower than the free stream value (2.20) because of a slight

misalignement of the flat plate. The agreement between computed and measured distributions is shown to be very good especially in the fore part of the interaction. Downstream of the shock impingement point, the predicted pressure rise is steeper than the measured one. This was also noticed in other Navier-Stokes computations [21, 22].

Figure 12 shows very good agreement between computed and measured velocity profiles in the separation region and downstream. The discrepancy upstream may reflect the difficulty of obtaining measurements in this region of high gradient and close surface proximity. A .15 mm zero shift of the laser table would improve agreement, suggesting a partial explanation of the discrepancy (Fig.12a). Finally, Fig.14 shows the distribution of skin friction coefficients in the interaction. The computed separation and reattachment points are seen to be in close agreement with the experimental results. They are also reported in Fig.11 for comparison.

Conclusions

An experimental and computational study of low speed and high speed 2D separated laminar flows has been performed. The problems were the feasability of performing velocity measurements with a sufficient resolution close to a solid surface in attached and separated flow regions, and the ability of predict-'ng the high speed flow with an implicit Navier-Stokes code based on the algorithm of [5].

It was shown that velocity measurements could be performed with very small probe volumes to within 0.08 from the wall in the low speed case and 0.1 mm from the wall in the high speed case, thus enabling an accurate description of velocity profiles across thin laminar boundary layers.

Separation of the low speed flow over an elliptic cylinder was recorded upstream of the mid chord.

The incident shock wave laminar boundary layer interaction was shown to be nominally 2D, exhibiting an extended separation region (from $x/x_{sh}=0.775$ to $x/x_{sh}=1.250$). The maximum negative velocity was -22 ms^{-1}, i.e., 0.041 u_∞.

The Navier-Stokes code proved to accurately predict the flow field in terms of pressure distributions, velocity profiles and locations of separation and reattachment.

Acknowledgement

References

1. HAKKINEN,R.J.;GREBER,I.; TRILLING,L.;ABARBANEL,S. S.: The interaction of an oblique shock wave with a laminar boundary layer. NASA Memo 2-18-59W,March 1959.
2. BAROTH,E.C. & HOLT,M.: Investigation of supersonic separated flow in a compression corner by laser doppler anemometry. Experiments in Fluids, Vol. 1, No 4, 1983, pp 195-203.
3. GINOUX,J.J. & DEGREZ,G.: 3D skewed shock wave/ laminar boundary layer interaction : laminar and turbulent behavior. AFOSR Final Scient.Rep. Grant AFOSR 82-0051, December 1982.
4. DEGREZ,G. & GINOUX,J.J.: 3D skewed shock wave laminar boundary layer interaction at Mach 2.25. AIAA P 83-1755; to be published in AIAA J.; also VKI Preprint 1983-04.
5. BEAM,R.M. & WARMING,R.F.: An implicit factored scheme for the compressible Navier-Stokes equations. AIAA J., Vol. 16, No 4, April 1978, pp 393-402.
6. DEGREZ,G.: Numerical solution of a 3D skewed shock wave laminar boundary layer interaction. Paper to be presented at the 3rd Int.Conf.on Boundary and Interior Layers (BAIL III), Dublin, June 1984; also VKI Preprint 1984-17.
7. ARINA,R. & ESSERS,J.A.: A finite difference technique for laminar and turbulent compressible boundary layers. in VKI LS 1983-01, January 1983.
8. GINOUX,J.J. & DEGREZ,G.: Velocity measurements in a 3D shock wave laminar boundary layer interaction. Part I : Preliminary investigations. AFOSR Final Scient.Rep. Grant AFOSR 83-0273, August 1984. To be published.
9. BOCCADORO,C.H.:Investigation of an oblique shock wave/laminar boundary layer interaction using LDV. VKI Project Report to be published June 1984.
10. VORROPOULOS,G.:An experimental study of compressibility effects in the leading edge vortex of a delta wing at incidence using LDV. Ph.D.Thesis, U. Libre de Bruxelles, June 1983.
11. BURGIO, C.: Comparison between shock wave/boundary layer interactions caused by either incident shocks or ramps. VKI PR 70-266, June 1970.
12. GINOUX,J.J.: Supersonic separated flows over wedges and flares with emphasis on a method of detecting transition. VKI TN 47, August 1968.
13. PEYRET,R. & VIVIAND,H.: Computation of viscous compressible flows based on the Navier-Stokes equations. AGARDograph 212, September 1975.
14. BEAM,R.W. & WARMING,R.F.:Implicit numerical methods for the compressible Navier-Stokes and Euler equations. in VKI LS 1982-04, April 1982.
15. THOMAS,P.D.: Numerical method for predicting flow characteristics and performances of non axisymmetric nozzles -Theory. NASA CR 3147, 1979.
16. SCHLICHTING,H.: Boundary layer theory. New York, McGraw-Hill, 1979.
17. SCHUBAUER, G.B.: Air flow in separating boundary layer. NACA TR 527, 1935.
18. SCHUBAUER,G.B.:Air flow in the boundary layer of an elliptic cylinder. NACA TR 652, 1939.
19. HANKEY,W.L. & HOLDEN,M.S.:2D shock wave-boundary layer interactions in high speed flows. AGARDogr 203.
20. LEWIS,J.E.: Experimental investigation of supersonic, laminar, 2D boundary layer separation in a compression corner with and without cooling. Ph.D. Thesis, California Institute of Technology, 1967.
21. McCORMACK,R.W.: An efficient numerical method for solving the time dependent compressible Navier-Stokes equations at high Reynolds number. NASA TM X 73 129, July 1976.
22. CARTER,J.E.: Numerical solution of the Navier-Stokes equations for the supersonic laminar flow over a 2D compression corner. NASA TR R 385, 1972.

The viscous flux vectors of equation (1) are :

$$\hat{\sigma}^{(\xi)} = \mu J \begin{bmatrix} 0 \\ (\nabla\xi\cdot\nabla\xi)u_\xi + \frac{1}{3}\xi_x(\nabla\xi\cdot\vec{V}_\xi) \\ (\nabla\xi\cdot\nabla\xi)v_\xi + \frac{1}{3}\xi_y(\nabla\xi\cdot\vec{V}_\xi) \\ (\nabla\xi\cdot\nabla\xi)(T/(\gamma-1)Pr+V^2/2)_\xi + \frac{1}{3}\cdot(\vec{V}\cdot\nabla\xi)(\nabla\xi\cdot\vec{V}_\xi) \end{bmatrix} \tag{A1}$$

$$\hat{\sigma}^{(\xi)} = \mu J \begin{bmatrix} 0 \\ (\nabla\xi\cdot\nabla\eta)u_\eta + (\eta_x\nabla\xi - 2/3\,\xi_x\nabla\eta)\cdot\vec{V}_\eta \\ (\nabla\xi\cdot\nabla\eta)v_\eta + (\eta_y\nabla\xi - 2/3\,\xi_y\nabla\eta)\cdot\vec{V}_\eta \\ (\nabla\xi\cdot\nabla\eta)(T/(\gamma-1)Pr+V^2/2)_\eta + [(\vec{V}\cdot\nabla\eta)\nabla\xi - 2/3(\vec{V}\cdot\nabla\xi)\nabla\eta]\cdot\vec{V}_\eta \end{bmatrix} \tag{A2}$$

$$\hat{\theta}^{(\xi)} = \mu J \begin{bmatrix} 0 \\ (\nabla\eta\cdot\nabla\xi)u_\xi + (\xi_x\nabla\eta - 2/3\,\eta_x\nabla\xi)\cdot\vec{V}_\xi \\ (\nabla\eta\cdot\nabla\xi)v_\xi + (\xi_y\nabla\eta - 2/3\,\eta_y\nabla\xi)\cdot\vec{V}_\xi \\ (\nabla\eta\cdot\nabla\xi)(T/(\gamma-1)Pr+V^2/2)_\xi + [(\vec{V}\cdot\nabla\xi)\nabla\eta - 2/3(\vec{V}\cdot\nabla\eta)\nabla\xi]\cdot\vec{V}_\xi \end{bmatrix} \tag{A3}$$

$$\hat{\theta}^{(\eta)} = \mu J \begin{bmatrix} 0 \\ (\nabla\eta\cdot\nabla\eta)u_\eta + \frac{1}{3}\eta_x(\nabla\eta\cdot\vec{V}_\eta) \\ (\nabla\eta\cdot\nabla\eta)v_\eta + \frac{1}{3}\eta_y(\nabla\eta\cdot\vec{V}_\eta) \\ (\nabla\eta\cdot\nabla\eta)(T/(\gamma-1)Pr+V^2/2)_\eta + \frac{1}{3}(\vec{V}\cdot\nabla\eta)(\nabla\eta\cdot\vec{V}_\eta) \end{bmatrix} \tag{A4}$$

The $\hat{F}$ and $\hat{G}$ matrices of equation (6) are [15] :

$$\begin{bmatrix} k_0 & k_1 & k_2 & 0 \\ -u(k_1 u + k_2 v) + k_1\phi^2 & -(\gamma-2)k_1 u + k_0 + k_1 u + k_2 v & -(\gamma-1)k_1 v + k_2 u & (\gamma-1)k_1 \\ -v(k_1 u + k_2 v) + k_2\phi^2 & k_1 v - (\gamma-1)k_2 u & -(\gamma-2)k_2 v + k_0 + k_1 u + k_2 & (\gamma-1)k_2 \\ (k_1 u + k_2 v)(-\gamma E + 2\phi^2) & [\gamma E - \phi^2]k_1 - (\gamma-1)(uk_1 + vk_2)u & [\gamma E - \phi^2]k_2 - (\gamma-1)(uk_1 + vk_2)v & \gamma(k_1 u + k_2 v) + k_0 \end{bmatrix}$$

$\phi^2 = (\gamma-1)\, V^2/2$

for $\hat{F}$ $\quad k_0 = \xi_t,\ k_1 = \xi_x,\ k_2 = \xi_y$; and for $\hat{G}$ $\quad k_0 = \eta_t,\ k_1 = \eta_x,\ k_2 = \eta_y$

The $\hat{S}$ and $\hat{T}$ matrices of equation (7) are, if we neglect any dependence of μ on $\hat{q}$

$$\hat{S} = \mu J \begin{bmatrix} 0 & 0 & 0 & 0 \\ s_{21} & \alpha_1 \left(\frac{1}{\hat{\rho}}\right)_\xi & \alpha_2 \left(\frac{1}{\hat{\rho}}\right)_\xi & 0 \\ s_{31} & \alpha_2 \left(\frac{1}{\hat{\rho}}\right)_\xi & \alpha_3 \left(\frac{1}{\hat{\rho}}\right)_\xi & 0 \\ s_{41} & s_{42} & s_{43} & s_{44} \end{bmatrix} \quad (C1)$$

$$\hat{T} = \mu J \begin{bmatrix} 0 & 0 & 0 & 0 \\ t_{21} & \alpha_1 \left(\frac{1}{\hat{\rho}}\right)_\eta & \alpha_2 \left(\frac{1}{\hat{\rho}}\right)_\eta & 0 \\ t_{31} & \alpha_2 \left(\frac{1}{\hat{\rho}}\right)_\eta & \alpha_3 \left(\frac{1}{\hat{\rho}}\right)_\eta & 0 \\ t_{41} & t_{42} & t_{43} & t_{44} \end{bmatrix} \quad (C2)$$

with

$s_{21} = -\alpha_1 (u/\hat{\rho})_\xi - \alpha_2 (v/\hat{\rho})_\xi$

$s_{31} = -\alpha_2 (u/\hat{\rho})_\xi - \alpha_3 (v/\hat{\rho})_\xi$

$s_{41} = \alpha_4 (-E/\hat{\rho} + V^2/\hat{\rho})_\xi - \alpha_1 (u^2/\hat{\rho})_\xi$
$\qquad - 2\alpha_2 (uv/\hat{\rho})_\xi - \alpha_3 (v^2/\hat{\rho})_\xi$

$s_{42} = -\alpha_4 (u/\hat{\rho})_\xi - s_{21}$

$s_{43} = -\alpha_4 (v/\hat{\rho})_\xi - s_{31}$

$s_{44} = \alpha_4 (1/\hat{\rho})_\xi$

$\alpha_1 = \xi_x^2/3 + (\nabla\xi)^2$

$\alpha_2 = \xi_x \xi_y/3$

$\alpha_3 = \xi_y^2/3 + (\nabla\xi)^2$

$\alpha_4 = \gamma/Pr \cdot (\nabla\xi)^2$

$t_{21} = -\alpha_1 (u/\hat{\rho})_\eta - \alpha_2 (v/\hat{\rho})_\eta$

$t_{31} = -\alpha_2 (u/\hat{\rho})_\eta - \alpha_3 (v/\hat{\rho})_\eta$

$t_{41} = \alpha_4 (-E/\hat{\rho} + V^2/\hat{\rho})_\eta - \alpha_1 (u^2/\hat{\rho})_\eta$
$\qquad - 2\alpha_2 (uv/\hat{\rho})_\eta - \alpha_3 (v^2/\hat{\rho})_\eta$

$t_{42} = -\alpha_4 (u/\hat{\rho})_\eta - t_{21}$

$t_{43} = -\alpha_4 (v/\hat{\rho})_\eta - t_{31}$

$t_{44} = \alpha_4 (1/\hat{\rho})_\eta$

$\alpha_1 = \eta_x^2/3 + (\nabla\eta)^2$

$\alpha_2 = \eta_x \eta_y/3$

$\alpha_3 = \eta_y^2/3 + (\nabla\eta)^2$

$\alpha_4 = \gamma/Pr (\nabla\eta)^2$

			Low speed	High speed
Beam separation, d		λ	0.6329 μm	0.5145 μm
Focal length, f		d	35 mm	50 mm
Beam diameter, D_{e-2}		D_{e-2}	2.49 mm	3.40 mm
Laser wavelength, λ		f	200 mm	750 mm
Angle of intersection, 2ϕ	$\phi = \arctan(d/2f)$	ϕ	5.0°	1.9°
Interfringe distance, d_f	$d_f = \lambda/2\sin\phi$	d_f	3.63 μm	7.72 μm
Beam waist, d_{e-2}	$d_{e-2} = 4\lambda f/\pi D_{e-2}$	d_{e-2}	64.7 μm	144 μm
Width of probe volume, d_m	$d_m = d_{e-2}/\cos\phi$	d_m	65.0 μm	144 μm
Length of probe volume, ℓ_m	$\ell_m = d_{e-2}/\sin\phi$	ℓ_m	0.743 mm	4.33 mm
Number of fringes, N_{fr}	$N_{fr} = d_m/d_f \cong \dfrac{4d}{\pi D_{e-2}}$	N_{fr}	17.9	18.7

TABLE 1 - LASER DOPPLER VELOCIMETRY PARAMETERS AND EQUATIONS
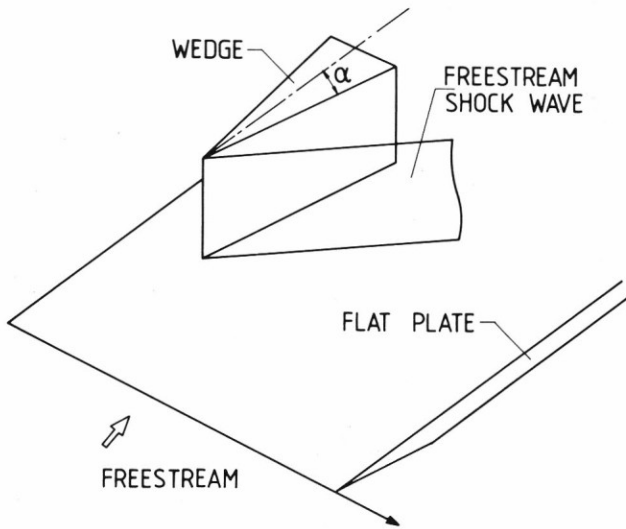
FIG. 1 - SCHEMATIC OF A 3D SKEWED SHOCK WAVE
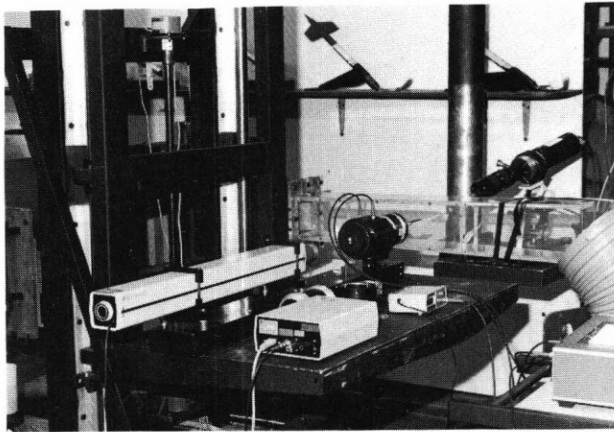BOUNDARY LAYER INTERACTION

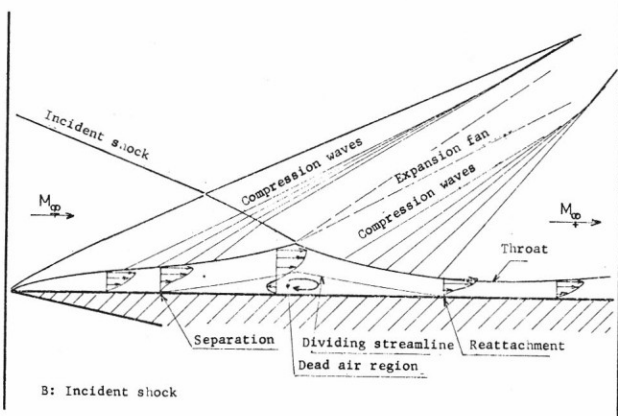FIG. 2 - LDV SETUP FOR LOW SPEED MEASUREMENTS

FIG. 3 - SCHEMATIC OF 2D INCIDENT SHOCK WAVE
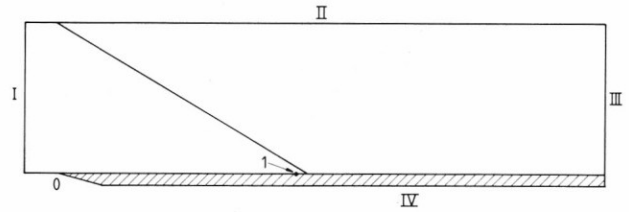LAMINAR BOUNDARY LAYER INTERACTION

FIG. 4 - COMPUTATIONAL DOMAIN FOR SHOCK WAVE/
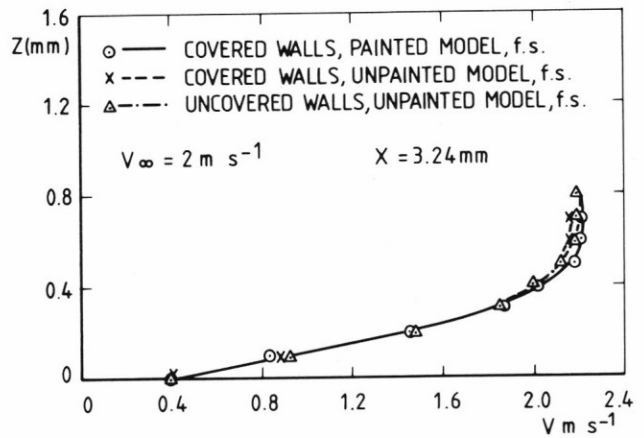BOUNDARY LAYER INTERACTION

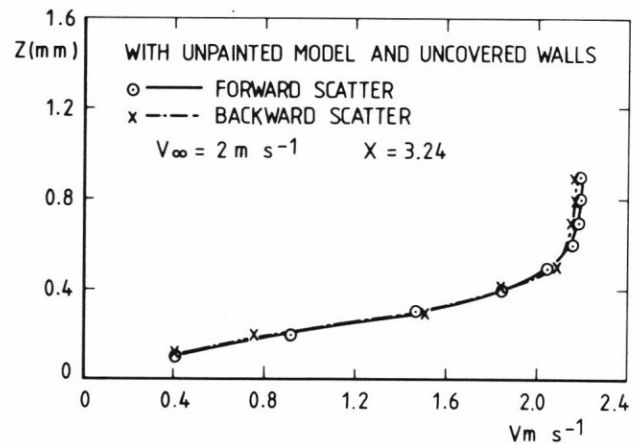FIG. 5 - VELOCITY MEASUREMENTS UNDER VARIOUS
EXPERIMENTAL CONDITIONS (ELLIPSE)

FIG. 6 - COMPARISON OF VELOCITY MEASUREMENTS USING
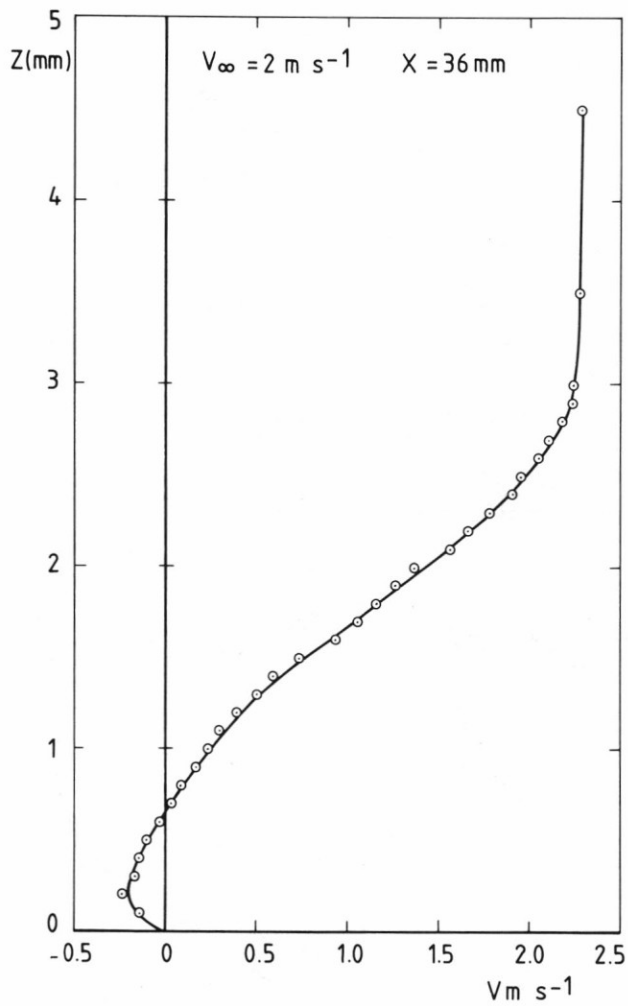FORWARD AND BACKSCATTER MODES (ELLIPSE)

FIG. 7 - VELOCITY PROFILE IN THE SEPARATED REGION
(WITH BRAGG CELLS) (ELLIPSE)
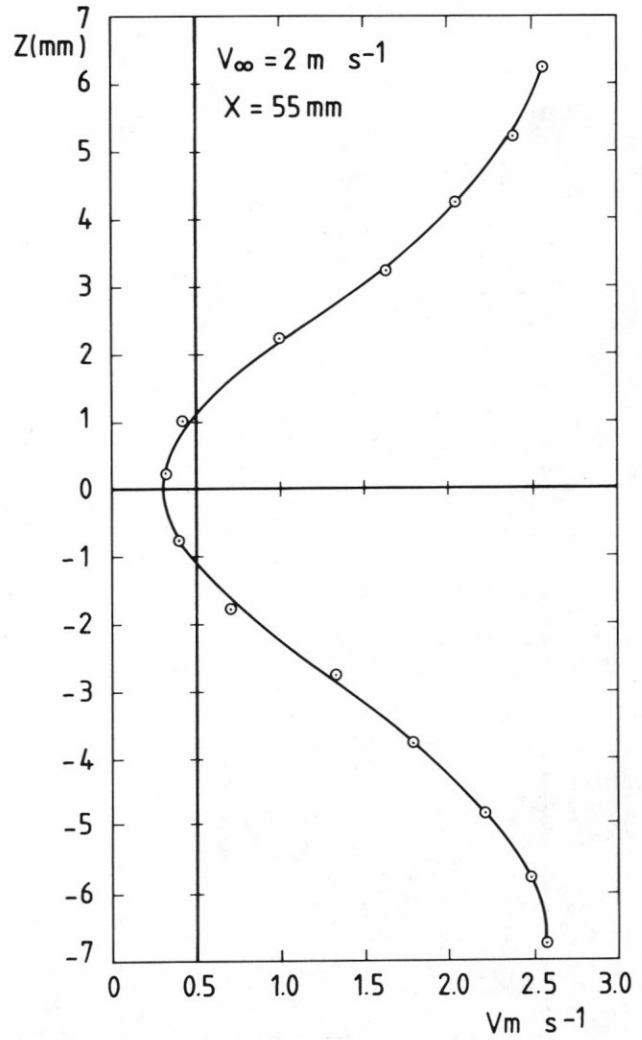
FIG. 8 - VELOCITY PROFILE IN THE WAKE (ELLIPSE)
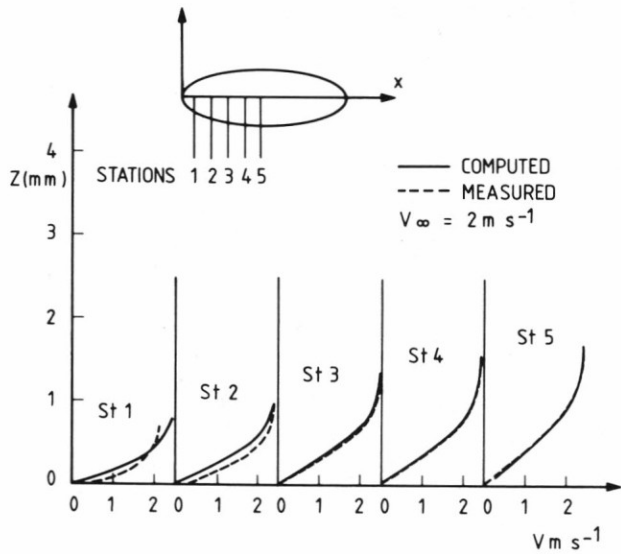
FIG. 9 - COMPARISON OF VELOCITY PROFILES MEASURED
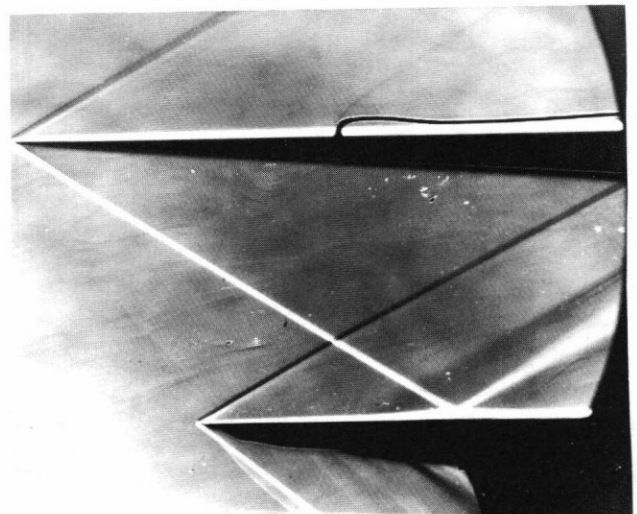AND BOUNDARY LAYER COMPUTATIONS

FIG. 10 - SCHLIEREN VISUALIZATION OF SHOCK WAVE/
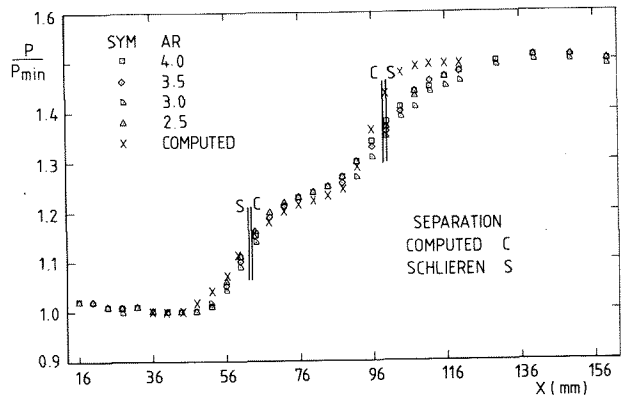BOUNDARY LAYER INTERACTION

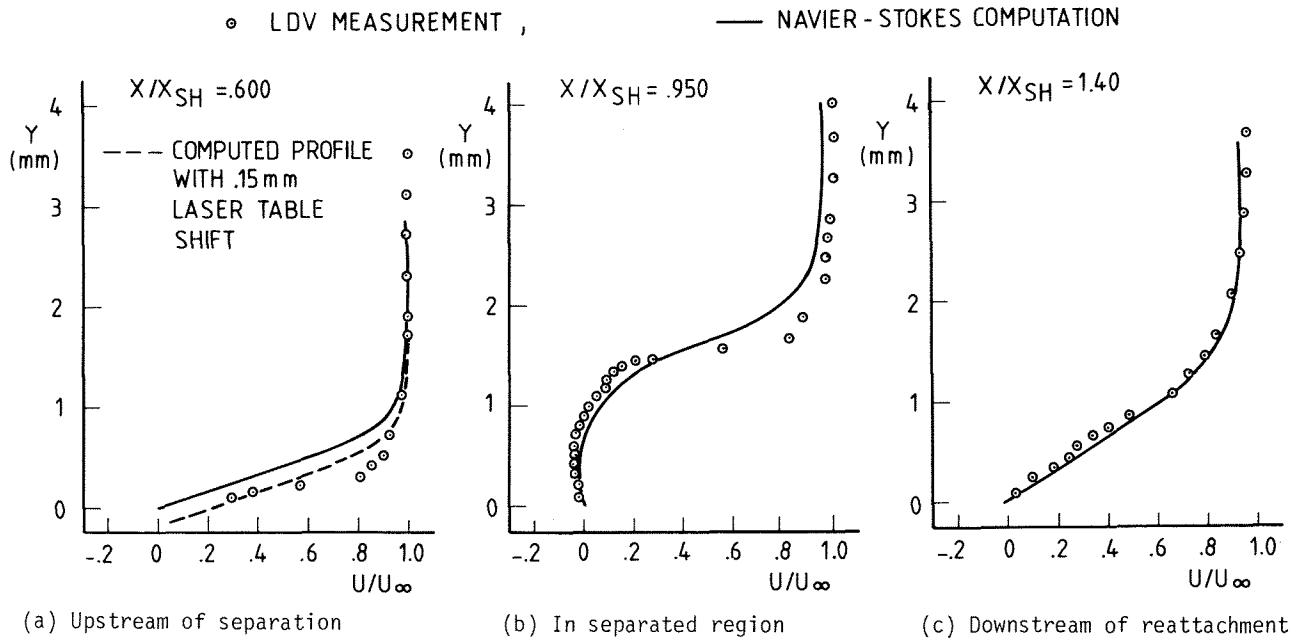FIG. 11 - PRESSURE DISTRIBUTION IN SHOCK WAVE/BOUNDARY LAYER INTERACTION

⊙ LDV MEASUREMENT , ——— NAVIER-STOKES COMPUTATION

(a) Upstream of separation   (b) In separated region   (c) Downstream of reattachment

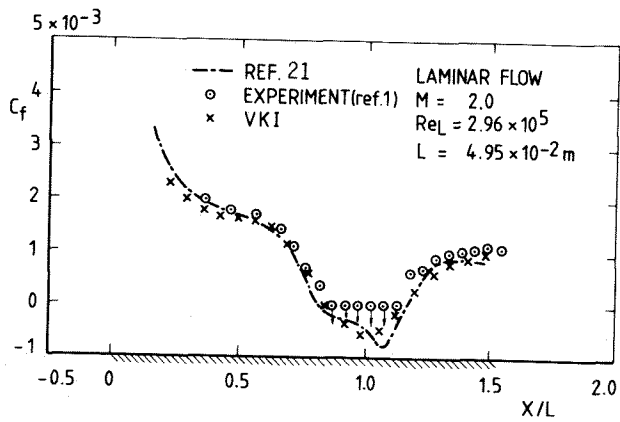FIG. 12 - VELOCITY PROFILES IN SHOCK WAVE/BOUNDARY LAYER INTERACTION

FIG. 13 - COMPARISON OF COMPUTATIONAL AND EXPERI-
MENTAL SKIN FRICTION COEFFICIENT DISTRIBUTION IN
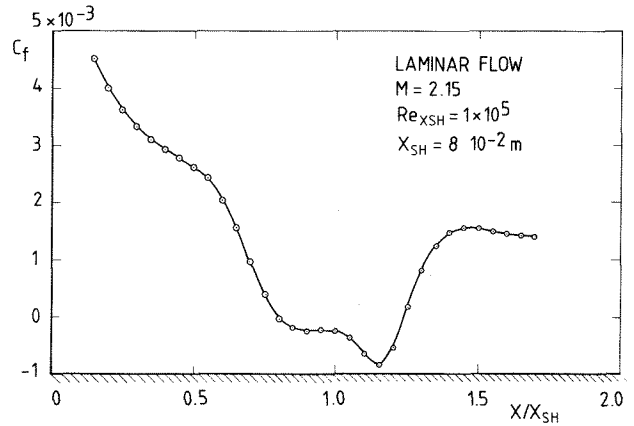SHOCK WAVE/BOUNDARY LAYER INTERACTION

FIG. 14 - COMPUTED SKIN FRICTION COEFFICIENT DIS-
TRIBUTION IN SHOCK WAVE/BOUNDARY LAYER INTERACTION
(PRESENT CONDITIONS)

296